Available online at www.sciencedirect.com
ScienceDirect
Engineering Fracture Mechanics 74 (2007) 314–331
Engineering Fracture Mechanics
www.elsevier.com/locate/engfracmech

# SGBEM analysis of crack–particle(s) interactions due to elastic constants mismatch

R.C. Williams [a], A.-V. Phan [a,*], H.V. Tippur [b], T. Kaplan [c], L.J. Gray [c]

[a] *Department of Mechanical Engineering, University of South Alabama, Mobile, AL 36688, USA*
[b] *Department of Mechanical Engineering, Auburn University, Auburn, AL 36849, USA*
[c] *Computer Science and Mathematics Division, Oak Ridge National Laboratory, Oak Ridge, TN 37831, USA*

Received 7 March 2006; received in revised form 26 May 2006; accepted 9 June 2006
Available online 25 July 2006

**Abstract**

The effects of elastic constants mismatch on the interaction between a propagating crack and single or multiple inclusions in brittle matrix materials are investigated using numerical simulations. The simulations employ a quasi-static crack-growth prediction tool based upon the symmetric-Galerkin boundary element method (SGBEM) for multiregions, a modified quarter-point crack-tip element, the displacement correlation technique for evaluating stress intensity factors (SIFs), and the maximum principal stress criterion for crack-growth direction. It is shown that, even with this simple method for calculating SIF, the crack-growth prediction tool is both highly accurate and computationally effective. This is evidenced by results for the case of a single inclusion in an infinite plate, where the SGBEM results for the SIFs show excellent agreement with known analytical solutions. The simulation results for crack growth and stress intensity behaviors in particulate media are very stable. The crack-tip shielding and amplification behaviors, as seen in similar studies using other numerical approaches, can be clearly observed.
© 2006 Elsevier Ltd. All rights reserved.

*Keywords:* Quasi-static crack growth; Crack–inclusion(s) interaction; Symmetric-Galerkin boundary element method

## 1. Introduction

Understanding the fracture properties of materials is vitally important to developing high performance composites for technological applications. While there has been a great deal of analytical and experimental exploration done in the area of crack–particle interactions, a literature review shows there are still relatively limited numerical studies available.

Analytical approaches have been developed for problems concerning cracks inside, outside, penetrating or lying along the interface of various types of inclusions (e.g., [1–3]). Numerical techniques, including finite

* Corresponding author. Tel.: +1 251 460 7453; fax: +1 251 460 6549.
*E-mail address:* vphan@jaguar1.usouthal.edu (A.-V. Phan).

0013-7944/$ - see front matter © 2006 Elsevier Ltd. All rights reserved.
doi:10.1016/j.engfracmech.2006.06.004

element methods (e.g., [4–8]) and boundary element methods (BEM) (e.g., [9–11]), have also been employed to investigate this type of fracture behavior under static loading conditions. Recently, the dynamic response of the interaction between a crack and an inclusion using the time-domain BEM has been studied by Lei et al. [12]. Bush [9] used a dual BEM (DBEM) to investigate the effects of particle size and orientation/location on crack path behavior and energetics. Both a single and an aggregate of particles were considered. A cursory analysis on the effects of a Young's modulus mismatch for a single particle was made. The accuracy of the numerical method used was validated by comparing simulation results for a tensile specimen without reinforcement to available analytical data for the same problem. Knight et al. [10] used DBEM to study the effects of a material property mismatch in a material with a single particle. The analysis focused on the effects of Poisson's ratio on energetics with only a brief consideration of Young's modulus effects. The validation was made by comparing simulation results for a non-reinforced tensile specimen to those of [9]. DBEM was also employed in the work by Wang et al. [11] to investigate the effects of elastic constant mismatch in a two-phase composite on crack extension paths.

The key feature of the BEM is that only the boundary of the domain is discretized. As a result, for fracture analysis, the singular stress field ahead of the crack is not approximated, and moreover, remeshing a propagating crack is easier. It is generally recognized that the BEM is particularly well suited for linear elastic fracture mechanics, as the method is known to provide more accurate results for stress (i.e., [13]) and there is no need for re-meshing the outer boundary during the modeling of crack propagation. Note that the BEM and the DBEM employ a collocation approximation at either boundary nodes or internal nodes (internal collocation). The main disadvantage associated with the sub-domain BEM technique for fracture [14] is the additional computational effort due to the use of an artificial interface along a crack; the major drawback of the DBEM is that the relaxation of continuity requirements at element boundaries and junctions will lead to singularities in the stress field in the vicinity of these points. If multiple, closely spaced crack assemblies are to be analyzed, this can, in certain cases, lead to numerical difficulties.

A variant of the BEM employing a Galerkin approximation, SGBEM [15,16] has several key advantages in fracture applications: (a) SGBEM uses the displacement boundary integral equation (BIE) on the boundary part where displacement is prescribed and traction BIE on the boundary part where traction is known. As the name implies, this results in a symmetric coefficient matrix, and this remains true for fracture problems providing that the unknowns on the crack faces are the crack opening displacement (COD); (b) the presence of both displacement and traction BIE enables fracture problems to be solved without using artificial subdomains; (c) unlike collocation, there is no smoothness requirement on the displacement (e.g., [17,18]) in order to evaluate the hypersingular integral; thus, standard continuous elements can be employed. The Galerkin approach can therefore easily exploit the highly effective quarter-point quadratic element to accurately capture the crack tip behavior; and (d) the weighted averaging formulation of Galerkin, by avoiding direct collocation at corners and junction points, provides a smoother solution in the neighborhood of geometric discontinuities.

In both finite and boundary element modeling of discrete cracks, the standard approach consists of incorporating the critical stress singularity and $\sqrt{r}$ displacement behavior at the crack tip by means of the quarter-point (QP) element [19,20], where $r$ is the distance from the crack tip. Use of this QP element at the crack tip has significantly improved the accuracy of SIF calculations (e.g., [14,21]). Nevertheless, in either finite or boundary element analyses, the prediction of $K_{II}$ and $K_{III}$ has not been nearly as accurate as for $K_I$. Recently, Gray and Paulino [22] have proved that, for an arbitrary crack geometry, a constraint exists in the series expansion of the crack opening displacement at the tip. As discussed in [22], the QP element in general fails to satisfy this constraint, and this has led to the development of an improved modified quarter-point (MQP) element [23]. It was demonstrated in [23] that the accuracy of the computed SIFs using a simple method, such as the Displacement Correlation Technique (DCT), can be significantly improved by incorporating this MQP element into the SGBEM. This implies that SIF-based criteria for crack growth direction, such as the maximum principal stress criterion (MPSC) [24], can be utilized in conjunction with the SGBEM for multiregions, the MQP crack-tip element, and the DCT to create an effective prediction tool for quasi-static crack-growth in particulate media.

The objectives of this paper are to demonstrate the performance of the aforementioned crack-growth prediction tool through numerical validation tests, and to study of effects of elastic constants mismatch on the interaction between a propagating crack and a single inclusion or multiple inclusions in a brittle matrix.

## 2. SGBEM-based crack-growth prediction tool

### 2.1. SGBEM

This section provides a very brief review of boundary integral equations for elasticity, their approximation via the symmetric-Galerkin procedure, and the application to fracture. The reader is asked to consult the cited references for further details.

The boundary integral equation (BIE) without body forces for linear elasticity is given by Rizzo [25]. For a source point $P$ interior to the domain, this equation takes the form

$$u_k(P) - \int_{\Gamma_b} \left[U_{kj}(P,Q)t_j(Q) - T_{kj}(P,Q)u_j(Q)\right] \mathrm{d}Q = 0, \tag{1}$$

where $Q$ is a field point, $t_j$ and $u_j$ are traction and displacement vectors, $U_{kj}$ and $T_{kj}$ are the Kelvin kernel tensors, $\Gamma_b$ denotes the boundary of the domain, and $\mathrm{d}Q$ is an infinitesimal boundary length (for 2-D) or boundary area (for 3-D cases). It can be shown that the limit of the integral in Eq. (1) as $P \to \Gamma_b$ exists. From now on, for $P \in \Gamma_b$, the BIE, and the singular integrals, are understood in this limiting sense.

For $P$ is off the boundary, the kernel functions are not singular and it is permissible to differentiate Eq. (1) with respect to $P$, yielding the hypersingular BIE (HBIE) for displacement gradient. Substitution of this gradient into Hooke's law gives the HBIE for boundary stresses

$$\sigma_{k\ell}(P) - \int_{\Gamma_b} \left[D_{kj\ell}(P,Q)t_j(Q) - S_{kj\ell}(P,Q)u_j(Q)\right] \mathrm{d}Q = 0. \tag{2}$$

Expressions for the kernel tensors $U_{kj}$,$T_{kj}$, $D_{kj\ell}$ and $S_{kj\ell}$ can be found in [15].

The Galerkin boundary integral formulation is obtained by taking the shape functions $\psi_m$ employed in approximating the boundary tractions and displacements as weighting functions for Eqs. (1) and (2). Thus,

$$\int_{\Gamma_b} \psi_m(P)u_k(P)\mathrm{d}P - \int_{\Gamma_b} \psi_m(P) \int_{\Gamma_b} [U_{kj}(P,Q)t_j(Q) - T_{kj}(P,Q)u_j(Q)]\mathrm{d}Q\ \mathrm{d}P = 0, \tag{3}$$

$$\int_{\Gamma_b} \psi_m(P)\sigma_{k\ell}(P)\mathrm{d}P - \int_{\Gamma_b} \psi_m(P) \int_{\Gamma_b} [D_{kj\ell}(P,Q)t_j(Q) - S_{kj\ell}(P,Q)u_j(Q)]\mathrm{d}Q\ \mathrm{d}P = 0. \tag{4}$$

A symmetric coefficient matrix, and hence a symmetric-Galerkin approximation, is obtained by employing Eq. (3) on the boundary $\Gamma_{b(\mathbf{u})}$ where displacements $u_{bv}$ are prescribed, and by using Eq. (4) on the boundary $\Gamma_{b(\mathbf{t})}$ with prescribed tractions $t_{bv}$. Note that $\Gamma_b = \Gamma_{b(\mathbf{u})} + \Gamma_{b(\mathbf{t})}$.

A solution procedure that employs a collocation approach enforces the integral Eqs. (1,2) at discrete source points whereas with Galerkin these equations are satisfied in an averaged sense. The additional boundary integration is the key to obtaining a symmetric coefficient matrix, as this ensures that the source point $P$ and field point $Q$ are treated in the same manner in evaluating the kernel tensors $U_{kj}$, $T_{kj}$, $D_{kj\ell}$ and $S_{kj\ell}$. After discretization, the resulting equation system can be written as

$$\begin{bmatrix} H_{11} & H_{12} \\ H_{21} & H_{22} \end{bmatrix} \begin{Bmatrix} u_{bv} \\ u \end{Bmatrix} = \begin{bmatrix} G_{11} & G_{12} \\ G_{21} & G_{22} \end{bmatrix} \begin{Bmatrix} t \\ t_{bv} \end{Bmatrix}. \tag{5}$$

Here, the first and second rows represent, respectively, the BIE written on ($\Gamma_{b(\mathbf{u})}$) and the HBIE on ($\Gamma_{b(\mathbf{t})}$). Further, $\mathbf{u}$ and $\mathbf{t}$ denote unknown displacement and traction vectors. Rearranging Eq. (5) into the form $[A]\{x\} = \{b\}$, and multiplying the HBIE by $-1$, one obtains

$$\begin{bmatrix} -G_{11} & H_{12} \\ G_{21} & -H_{22} \end{bmatrix} \begin{Bmatrix} t \\ u \end{Bmatrix} = \begin{Bmatrix} -H_{11}u_{bv} + G_{12}t_{bv} \\ H_{21}u_{bv} - G_{22}t_{bv} \end{Bmatrix} \tag{6}$$

The symmetry of the coefficient matrix, $G_{11} = G_{11}^{\mathrm{T}}$, $H_{22} = H_{22}^{\mathrm{T}}$ and $H_{12} = G_{21}^{\mathrm{T}}$ now follows from the symmetry properties of the kernel tensors.

The above SGBEM formulations need to be extended to deal with multiregion problems involved in particulate materials. The technique is based on the assumption of a perfect bonding between inclusions and the

matrix which results in the displacement continuity and equilibrium conditions across the interfaces. More details of the multiregion SGBEM can be found in, e.g., [26–28].

### 2.2. SGBEM fracture analysis

Consider a finite domain or body, B, of general shape as shown in Fig. 1. The body is shown to include a crack surface denoted as $\Gamma_c$ on which only tractions are prescribed. Initially, the crack is composed of two coincident surfaces according to $\Gamma_c = \Gamma_c^+ + \Gamma_c^-$ where $\Gamma_c^+$ and $\Gamma_c^-$ denote the upper and lower crack surfaces, respectively. As a result, the outward normals to the crack surfaces, $\mathbf{n}_c^+$ and $\mathbf{n}_c^-$, are oriented oppositely so that $\mathbf{n}_c^- = -\mathbf{n}_c^+$. If the displacements $\mathbf{u}_c^+$ and $\mathbf{u}_c^-$ are replaced by the COD $\Delta\mathbf{u}_c = \mathbf{u}_c^+ - \mathbf{u}_c^-$, and the tractions $\mathbf{t}_c^+$ and $\mathbf{t}_c^-$ by the sum of tractions $\Sigma\mathbf{t}_c = \mathbf{t}_c^+ + \mathbf{t}_c^-$ ($\Sigma\mathbf{t}_c = 0$ as the crack surfaces are assumed to be symmetrically loaded), the BIE and HBIE written for an interior point $P$ then take the following forms:

$$u_k(P) = \int_{\Gamma_b} \left[U_{kj}(P,Q)t_j(Q) - T_{kj}(P,Q)u_j(Q)\right]\mathrm{d}Q - \int_{\Gamma_c^+} T_{kj}(P,Q)\Delta u_j(Q)\mathrm{d}Q, \tag{7}$$

$$\sigma_{k\ell}(P) = \int_{\Gamma_b} \left[D_{kj\ell}(P,Q)t_j(Q) - S_{kj\ell}(P,Q)u_j(Q)\right]\mathrm{d}Q - \int_{\Gamma_c^+} S_{kj\ell}(P,Q)\Delta u_j(Q)\mathrm{d}Q. \tag{8}$$

It can be shown that a symmetric coefficient matrix results from this choice of $\Delta\mathbf{u}$ as variables on $\Gamma_c^+$. Following the Galerkin approximation, the limit of Eqs. (7) and (8) is taken as $P \to \Gamma_{b(\mathbf{u})}$ and $\Gamma_{b(\mathbf{t})}$, respectively. At this point, it is convenient to convert the stress Eq. (8) into a traction equation through Cauchy's relation $t_k(P) = \sigma_{\ell k}(P)\, n_\ell(P)$, with $n_\ell(P)$ being the outward normal at $P$. After discretizing, the system resulting from Eqs. (7) and (8) is

$$[G_{bb}]\{t_b\} = [H_{bb}]\{u_b\} + [H_{bc}]\{\Delta u_c\}, \tag{9}$$

where $b$ and $c$ denote the outer boundary and upper crack surface, respectively.

As traction boundary conditions are prescribed on the crack, only Eq. (8) is written for source points on $\Gamma_c^+$. Again, following the Galerkin approximation, the limit of Eq. (8) as $P \to \Gamma_c$, the conversion of Eq. (8) into a traction equation, and discretization, the result is

$$[G_{cb}]\{t_b\} - [G_{cc}]\{t_c^+\} = [H_{cb}]\{u_b\} + [H_{cc}]\{\Delta u_c\}. \tag{10}$$

Combining Eqs. (9) and (10), the system of equations can be written as

$$\begin{bmatrix} H_{bb} & H_{bc} \\ H_{cb} & H_{cc} \end{bmatrix} \begin{Bmatrix} u_b \\ \Delta u_c \end{Bmatrix} = \begin{bmatrix} G_{bb} & 0 \\ G_{cb} & G_{cc} \end{bmatrix} \begin{Bmatrix} t_b \\ -t_c^+ \end{Bmatrix}, \tag{11}$$

where it can be proved that the coefficient matrix on the left hand side of Eq. (11) is symmetric.

### 2.3. Modified quarter-point element

It has been proven that, irrespective of the crack problem geometry or boundary conditions, the series expansion for the COD $\Delta u_k$, $k = 1,2$ in the neighborhood of the tip is [22] (for related work see Refs. [29–31]),

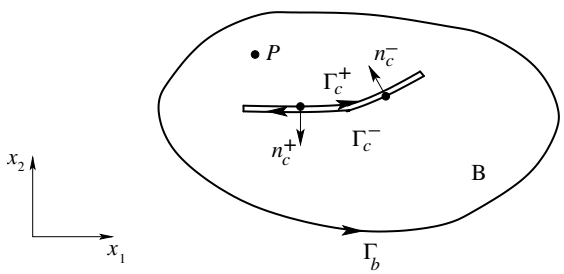


Fig. 1. A body B containing a fracture.

$$\Delta u_k(r,\theta) = b_k(\theta) r^{\frac{1}{2}} + d_k(\theta) r^{\frac{3}{2}} + \mathcal{O}\left(r^{\frac{5}{2}}\right), \tag{12}$$

where $r$,$\theta$ are the distance to, and the direction emanating from, the tip, respectively.

The 2-D QP element is based upon the three-equidistant-noded quadratic element. For $\xi \in [0,1]$, the shape functions for this element are given by

$$\begin{aligned} \psi_1(\xi) &= (1-\xi)(1-2\xi), \\ \psi_2(\xi) &= 4\xi(1-\xi), \\ \psi_3(\xi) &= \xi(2\xi-1). \end{aligned} \tag{13}$$

Since $\Delta\mathbf{u} = 0$ at the crack tip, which is assumed to be at $\xi = 0$ (Fig. 2) the geometry and COD representations of the crack tip element are

$$\Gamma(\xi) = \sum_{j=1}^{3} \left(x_j \psi_j(\xi), y_j \psi_j(\xi)\right), \tag{14}$$

$$\Delta u_k(\xi) = \sum_{j=2}^{3} \left(\Delta u_1^{(j)} \psi_j(\xi), \Delta u_2^{(j)} \psi_j(\xi)\right), \tag{15}$$

where $(x_j, y_j)$ are the coordinates of the three nodes defining the crack tip element, and $\Delta u_k^{(j)}$ the nodal values of the COD.

By moving the mid-node coordinates $(x_2, y_2)$ three-fourths of the way towards the tip (see Fig. 2), the parameter $\xi$ becomes $\sqrt{r/L}$, with $L$ being the distance from $(x_1, y_1)$ to $(x_3, y_3)$ [19,20]. As a consequence, the leading order term in $\Delta u_k^{(j)}$ at $\xi = 0$, which is $\xi$, is the correct square root of distance. Note however, that the next term, which is $\xi^2$, is $r/L$. According to Eq. (12), this term should vanish, and the modification presented in Ref. [23] accomplishes the cancellation of this $\xi^2$ term. The resulting shape functions for the MQP element are

$$\begin{aligned} \hat{\psi}_2(\xi) &= -\frac{8}{3}(\xi^3 - \xi), \\ \hat{\psi}_3(\xi) &= \frac{1}{3}(4\xi^3 - \xi), \end{aligned} \tag{16}$$

which should be used in Eq. (15) instead of $\psi_j(\xi)$. It can be observed that the modified shape functions Eq. (16) still satisfy the Kronecker delta property $\hat{\psi}_i(\xi_j) = \delta_{ij}$. This new approximation is only applied to the COD, as we keep the representation of the crack tip geometry as in Eq. (14). This ensures that the property $\xi \sim \sqrt{r}$ remains.

### 2.4. Stress intensity factors by the DCT

There are several approaches for numerically evaluating SIFs. Among these approaches, the DCT based upon the COD in the vicinity of the crack tip is one of the simplest methods. For the MQP element, the DCT-based SIFs are given by [23]

$$\begin{aligned} K_{\mathrm{I}} &= \frac{G}{3(\kappa+1)} \sqrt{\frac{2\pi}{L}} \left(8\Delta u_2^{(2)} - \Delta u_2^{(3)}\right), \\ K_{\mathrm{II}} &= \frac{G}{3(\kappa+1)} \sqrt{\frac{2\pi}{L}} \left(8\Delta u_1^{(2)} - \Delta u_1^{(3)}\right), \end{aligned} \tag{17}$$

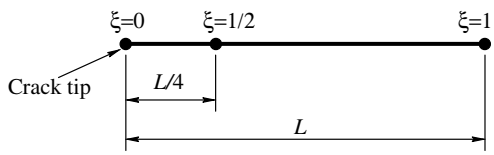


Fig. 2. Crack tip element.

where $\Delta u_i$ is the COD in the coordinate system associated with the crack tip under consideration, $G$ is the shear modulus, $\nu$ is Poisson's ratio, and

$$\kappa = 3 - 4\nu \text{ (plane strain)}, \quad \kappa = \frac{3-\nu}{1+\nu} \text{ (plane stress)}. \tag{18}$$

As SIFs are directly given in terms of the nodal values of the COD at the crack tip, and the MQP element enhances the accuracy of the nodal CODs, this enhances accuracy of the obtained SIFs.

### 2.5. Maximum principal stress criterion

There are several criteria for predicting crack growth direction (e.g., [24,32]). The MPSC proposed by Erdogan and Sih [24], which is a commonly used criterion, is adopted herein. According to this criterion, the crack growth direction is normal to the maximum principal stress $\sigma_\theta$. In other words, along the crack growth direction $\theta_c$, $\sigma_\theta$ is maximum and the shear stress $\sigma_{r\theta} = 0$, which leads to

$$K_{\mathrm{I}} \sin\theta_c + K_{\mathrm{II}}(3\cos\theta_c - 1) = 0. \tag{19}$$

It follows that,

$$\theta_c = 2\tan^{-1}\left(\frac{K_{\mathrm{I}}}{4K_{\mathrm{II}}} \pm \frac{1}{4}\sqrt{\left(\frac{K_{\mathrm{I}}}{K_{\mathrm{II}}}\right)^2 + 8}\right) \quad \text{and} \quad -\pi < \theta_c < \pi. \tag{20}$$

In this work, a quasi-static crack-growth prediction tool based upon the SGBEM for multiregions, the MQP crack-tip element, the DCT and the MPSC are combined to simulate the interaction between a crack and various types of inclusions embedded within polymer matrix composites. By incorporating the MQP shape functions (16) into a SGBEM code, accurate CODs $\Delta\mathbf{u}$ at the quarter-point and end nodes of any crack-tip element may be obtained (see Eq. (11)). The SIFs at the crack tip of interest will then be evaluated by substituting the related CODs in the DCT formulas Eq. (17). If $K_{\mathrm{I}} \geqslant K_{\mathrm{I}c}$, the crack will propagate. In this case, the growth direction $\theta_c$ of the crack tip in question is determined by Eq. (20) which is a function of $K_{\mathrm{I}}$ and $K_{\mathrm{II}}$. A new crack tip (quarter-point) element of length $\Delta a$ is added in that direction and on top of the previous crack tip element (which now becomes a regular element) during a growth simulation. Consequently, remeshing a propagating crack is straightforward as the previous element discretization remains unchanged. At issue is the determination of $\Delta a$ which has no formal constraint in quasi-static loading conditions. Smaller $\Delta a$, although leading to more time-consuming simulations, are expected to result in more accurate and stable simulations.

## 3. Simulation results and discussion

In this section we first validate the multiregion SGBEM code (with the MQP element) by comparing results to those produced by an analytical method; the test case consists of a single inclusion in an infinite medium. This code is then used to explore the role material constant mismatches play in crack growth-inclusion interactions. Simulations are run to examine crack growth behaviors and the mode-I SIF in a composite beam. The simulations consider cases of both a single and multiple inclusions. Here, the inclusion(s) are modeled as perfectly bonded to the surrounding matrix material, and both the inclusion(s) and the matrix are treated as isotropic, linear elastic materials under plane strain assumptions. Crack propagation takes place solely in the matrix material.

### 3.1. Crack–inclusion interaction in an infinite plate under tension

Hwu et al. [3] have developed a robust analytical model that can be used to investigate crack–particle interactions for several different types of problems. The case of an isotropic circular inclusion in an infinite isotropic medium under a uniaxial remote stress $\sigma$ is the problem of interest for this validation. The problem is illustrated in Fig. 3 where the inclusion radius is denoted by $r_v$. The coordinates $(x^o, y^o)$ of the midpoint $O$

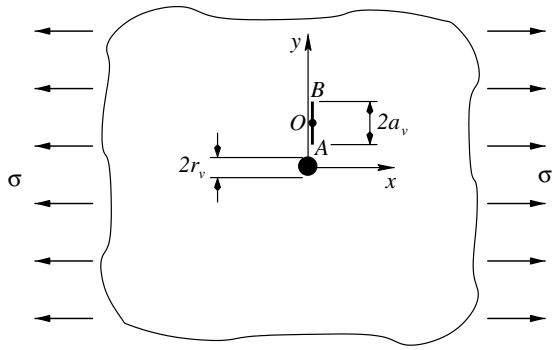


Fig. 3. Crack–inclusion interaction in an infinite plate under tension.

of the crack are measured with respect to the center of the inclusion, which has been arbitrarily given the coordinates of $(0,0)$. The crack length $2a_v$, exaggerated for clarity, is taken to be equivalent in length to the particle radius $r_v$ ($2a_v/r_v = 1$). Poisson's ratio and Young's modulus are respectively denoted by, $\nu_p$ and $E_p$ for the particle, and $\nu_m$ and $E_m$ for the matrix (plate). The values for the Young's moduli and Poisson's ratios, $E_p/E_m = 22.148148$, $\nu_p = 0.3$, and $\nu_m = 0.35$, are chosen to be consistent with Ref. [3].

In the verification model, the crack is initially positioned a distance $x^o/r_v = 0.5$, $y^o/r_v = 1.5$. Twenty-eight elements are used to mesh the particle boundary. The crack tip closest to the particle is denoted by $A$, while the opposite crack tip is denoted $B$ (corresponding to $-L$ and $+L$ of Ref. [3]). In subsequent simulations, the crack is moved away from the particle with its midpoint repositioned at different coordinates, using the same reference scheme for positioning described earlier. The coordinates for the crack midpoint $O$ are given in column 1 of Tables 1 and 2 . Simulations are run at each set of coordinates to find the normalized SIFs $K'_{\mathrm{I}}$ and $K'_{\mathrm{II}}$, which are defined as

$$K' = \frac{K}{\sigma\sqrt{\pi a_v}}, \tag{21}$$

at both ends of the crack. Tables 1 and 2 give our results compared to those of the analytical results from Ref. [3].

Table 1
Normalized stress intensity factors at crack tip $A$ ($K' = K/(\sigma\sqrt{\pi a_v})$)

| $\left(\frac{x^o}{r_v}, \frac{y^o}{r_v}\right)$ | $K'_{\mathrm{IA}}$ | | $K'_{\mathrm{IIA}}$ | |
|---|---|---|---|---|
| | SGBEM | Hwu et al. [3] | SGBEM | Hwu et al. [3] |
| (0.5, 1.5) | 0.614 | 0.613 | 0.055 | 0.061 |
| (0.5, 1.75) | 0.752 | 0.750 | −0.043 | −0.041 |
| (0.5, 2) | 0.835 | 0.834 | −0.062 | −0.062 |
| (0.5, 3) | 0.956 | 0.956 | −0.034 | −0.035 |
| (0.5, 4) | 0.982 | 0.982 | −0.016 | −0.016 |

Table 2
Normalized stress intensity factors at crack tip $B$ ($K' = K/(\sigma\sqrt{\pi a_v})$)

| $\left(\frac{x^o}{r_v}, \frac{y^o}{r_v}\right)$ | $K'_{\mathrm{IB}}$ | | $K'_{\mathrm{IIB}}$ | |
|---|---|---|---|---|
| | SGBEM | Hwu et al. [3] | SGBEM | Hwu et al. [3] |
| (0.5, 1.5) | 0.818 | 0.817 | −0.067 | −0.067 |
| (0.5, 1.75) | 0.878 | 0.878 | −0.062 | −0.062 |
| (0.5, 2) | 0.916 | 0.915 | −0.052 | −0.052 |
| (0.5, 3) | 0.972 | 0.973 | −0.024 | −0.024 |
| (0.5, 4) | 0.987 | 0.987 | −0.012 | −0.012 |

As can be seen from the tables, the results produced by the multiregion SGBEM code with MQP element are in very good agreement with the analytical results, even with a relatively coarse mesh. Because our model is based upon a numerical method, some error is to be expected, particularly when the crack tip is extremely close to the inclusion-matrix interface. A value of interest was $K'_{\mathrm{IIA}}$ at $(x^o/r_v, y^o/r_v) = (0.5, 1.5)$. There is roughly a 10% difference in our value for $K'_{\mathrm{II}}$ and the reference value at this point. However, another reference [33] used for comparison in Ref. [3] gives a value for $K'_{\mathrm{IIA}} = 0.057$ at the point in question, that is within 3% of our calculated value. The validation simulations indicate that our SGBEM code is capable of producing highly accurate results, even when the crack tip is extremely close to interface boundaries.

### 3.2. Effects of $E_p/E_m$ on single particle–crack interaction

The loading, constraints, and geometry of a three-point beam specimen shown in Fig. 4 are used for all material constant mismatch simulations that follow. Here $L \times h \times t = 0.150\ \mathrm{m} \times 0.04\ \mathrm{m} \times 0.008\ \mathrm{m}$ where $t$ is the beam thickness. The beam is subjected to a concentrated load $P$, and the crack length $a$ is selected to be equivalent to $h/4$. The changes in crack length in the $x$ and $y$ directions, $x_a$ and $y_a$, are normalized with respect to the half-length $L/2$, and the height $h$ of the beam, respectively. The materials are modeled as being linear elastic and isotropic. Plane strain conditions are assumed in all simulations. A normalized mode-I SIF is introduced and defined as

$$K'_{\mathrm{I}} = \frac{K_{\mathrm{I}}}{K_{\mathrm{Io}}}, \tag{22}$$

where $K_{\mathrm{Io}}$ is the mode-I SIF for the same problem without any particle present.

For simulations involving a single particle, an inclusion of radius $r = 0.001$ m is centered in the beam and offset an amount $-r$ from the $y$-axis (see Fig. 4). The inclusion is offset to facilitate the deflection due to inclusion location. For these as well as the following simulations, 193, 10, and 24 quadratic elements are employed to mesh the boundary of the beam (excluding the crack), the crack, and each particle, respectively. A relatively small amount of crack increment, namely $\Delta a/a = 0.03$, is used for all simulations to ensure the stability of subsequent crack growth steps.

In this section, effects of a Young's modulus mismatch between a single particle and its matrix on crack propagation are considered. For these simulations, $E_{\mathrm{m}}$ is kept constant while the values for $E_{\mathrm{p}}$ range from $2E_{\mathrm{m}}$ to $16E_{\mathrm{m}}$ and are increased by successive doublings. The Poisson's ratio for the matrix material and the particle, $\nu_{\mathrm{m}}$ and $\nu_{\mathrm{p}}$, are both equal to 0.3 and kept constant for all simulations. The results for the crack growth are shown in Fig. 5, while the results for the $K'_{\mathrm{I}}$ are shown in Fig. 6.

From Fig. 5, it is clear that the mismatch between $E_{\mathrm{p}}$ and $E_{\mathrm{m}}$ plays a prominent role in crack deflection. As $E_{\mathrm{p}}$ is increased, it can be seen that crack deflection away from the inclusion increases noticeably when the crack is in the immediate vicinity of the inclusion. Of interest is the observation that the amount of increase that occurs in the crack deflection does appear to potentially have a bounding value. The difference between the amounts of crack deflection from one value of $E_{\mathrm{p}}/E_{\mathrm{m}}$ to the next, as $E_{\mathrm{p}}/E_{\mathrm{m}}$ is increased, appears to be decreasing. Because of the asymmetrical support conditions the crack is expected to propagate by a very slight

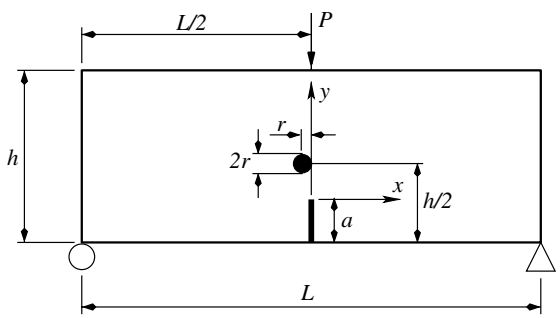


Fig. 4. Crack–inclusion interaction in a three-point beam specimen.

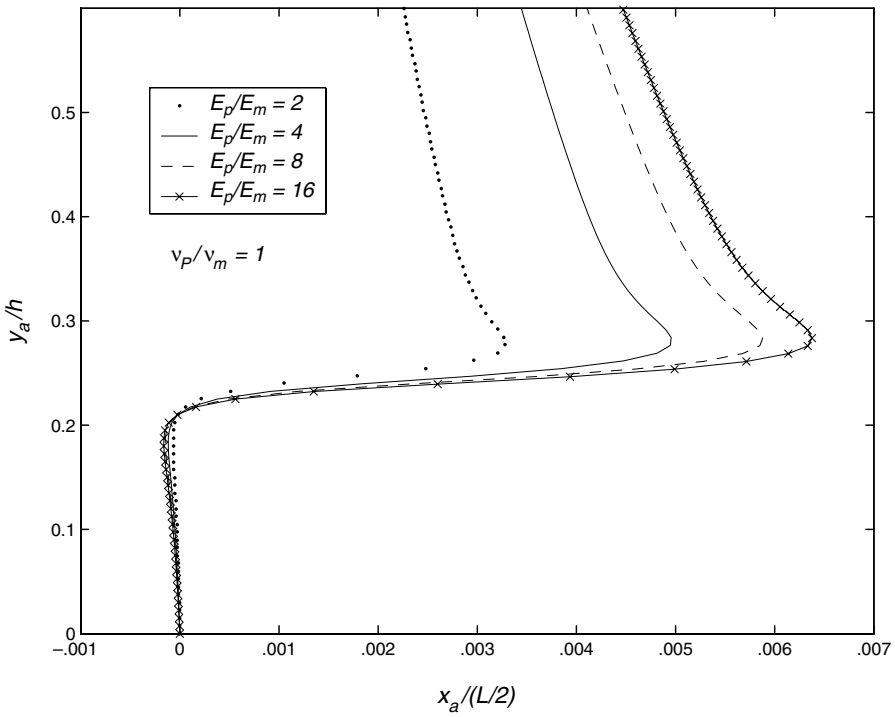


Fig. 5. Effects of $E_p/E_m$ on crack deflection due to single particle–crack interaction.

amount in the $-x$ direction, towards the roller constraint. Simulations run without an inclusion have demonstrated that to be the case. Increases in $E_p$ appear to cause small, but noticeable, increases in the deflection towards the roller support. The result implies that the inclusion may actually be attracting the crack when the crack is sufficiently far away from the inclusion, and that increasing the inclusion stiffness causes an increase in the aforementioned crack attraction.

The Mode-I SIF clearly shows a decrease in magnitude as the crack nears the inclusion followed by an increase in magnitude as the crack reaches, and subsequently passes, the inclusion. Once past the inclusion, $K_I$ undergoes another, less substantial, decrease in its magnitude. The initial $K_I$ reduction seems to be more substantial than the corresponding amount of amplification, in general. A stiffer inclusion increases the $K_I$ amplification and reduction that occur, and increasing $E_p$ appears to have a more substantial effect on $K_I$ reduction than $K_I$ amplification. The secondary $K_I$ reduction that occurs also experiences an increase with increasing $E_p$. However, the increase in the amount of secondary $K_I$ reduction is less considerable than that experienced by either the initial $K_I$ reduction or the $K_I$ amplification.

### 3.3. Effects of $\nu_p/\nu_m$ on single particle–crack interaction

Effects of a Poisson's ratio mismatch between a single inclusion and matrix material have also been explored. The Poisson's ratio effects are evaluated at $E_p/E_m = 2$ and $E_p/E_m = 16$, in order to cover cases of both relatively high and low $E_p/E_m$ ratios. In all simulations, the Poisson's ratio $\nu_m$ is selected to be 0.3 while $\nu_p$ takes the values 0.2, 0.3 and 0.4. Figs. 7 and 8 show the effects of $\nu_p$ on crack deflection for $E_p/E_m = 2$ and $E_p/E_m = 16$, respectively. Figs. 9 and 10 show the effects of $\nu_p$ on $K_I$ for $E_p/E_m = 2$ and $E_p/E_m = 16$, respectively. When $E_p/E_m$ is large, the crack deflection away from the inclusion varies only slightly as $\nu_p$ is increased. However, a notable increase in the deflection can clearly be seen for the lower value of $E_p/E_m$ as $\nu_p$ is increased. Crack attraction towards the inclusion when the crack is far away from the inclusion is in general lessened as $\nu_p$ is increased. As with crack deflection, the ratio $\nu_p/\nu_m$ is more influential on crack attraction at lower values of $E_p/E_m$. There does not seem to be any discernable change in the actual path of the crack deflection due to changes in $\nu_p/\nu_m$ relative to the Young's modulus simulations.

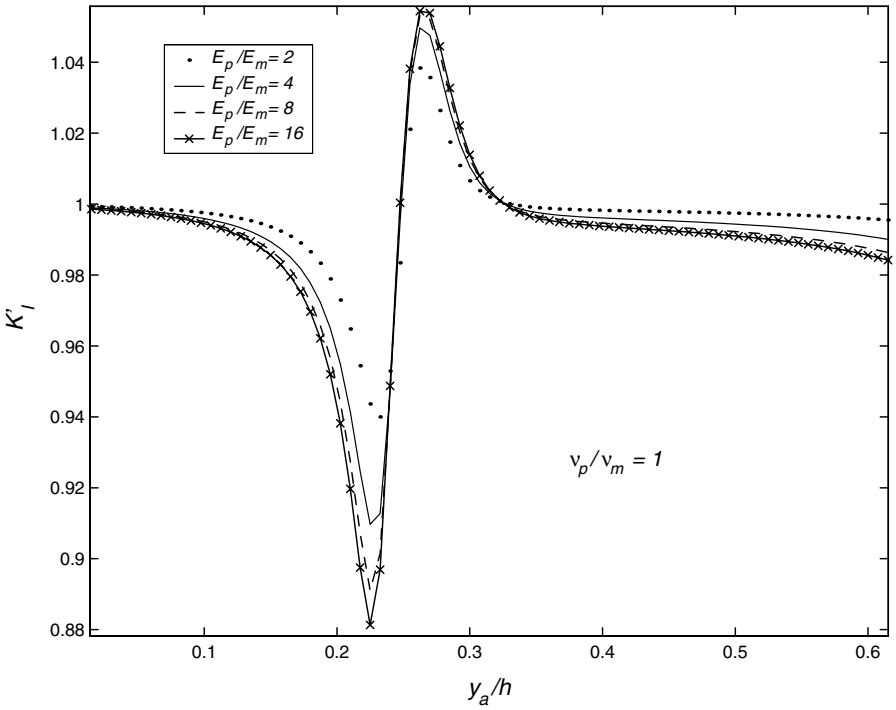


Fig. 6. Effects of $E_p/E_m$ on $K'_I$ due to single particle–crack interaction.

The pattern of $K_I$ amplification and reduction also remained unchanged from the previous simulations shown in Fig. 6. The magnitude of $K_I$ amplification and reduction, for both $E_p/E_m = 2$ and $E_p/E_m = 16$, are increased as $\nu_p$ is increased. Ratio $\nu_p/\nu_m$ has a considerably greater effect on $K_I$ for the lower value of $E_p/E_m$. It is also worth noting that, for the lower value of $E_p/E_m$, the $K_I$ curves appear to be more spread out (shifted horizontally) in the reduction portion of the curve than in the amplification portion. This result may imply that $\nu_p/\nu_m$ plays a more important role in $K_I$ reduction at least for small values of $E_p/E_m$. For the higher value of $E_p/E_m$, the amount of curve separation appeared essentially uniform between all portions of the curves.

### 3.4. Effects of $E_p/E_m$ on aggregate–crack interaction

Effects of a Young's modulus mismatch on a matrix material containing multiple inclusions (aggregate) are considered next. The values for $E_p$, $E_m$, $\nu_p$, $\nu_m$, and increment values (for $E_p$) are identical to those used in the single inclusion Young's modulus mismatch simulations. The geometry of the aggregate is shown in Fig. 11 where the center of the aggregate coincides with the center of the single particle in Fig. 4. Fig. 12 shows the variation in crack deflection with changing $E_p/E_m$ while Fig. 13 shows the variation in $K_I$ with changing $E_p/E_m$.

Comparing the single particle simulation results to the results given by [9], it could be said that increasing inclusion stiffness has a similar effect on crack deflection as increasing the inclusion size or decreasing the distance between the particle and crack. This assertion is useful in understanding and interpreting the results of the multiple inclusion simulation. Fig. 12 shows that the addition of inclusions to the beam material has a significant effect on the crack deflection pattern. Crack deflection away from the first inclusion encountered shows a larger and sharper peak for all values of $E_p/E_m$ relative to the results from the corresponding single inclusion simulations. The increase in crack deflection magnitude and sharpness is most easily attributed to the presence of a nearby particle, added deflection caused by one or both of the far particles, or a combination of the two effects. There are certainly other possible explanations but these are the most straightforward. The general deflection pattern indicates increasingly complex interactions between the crack and inclusions with

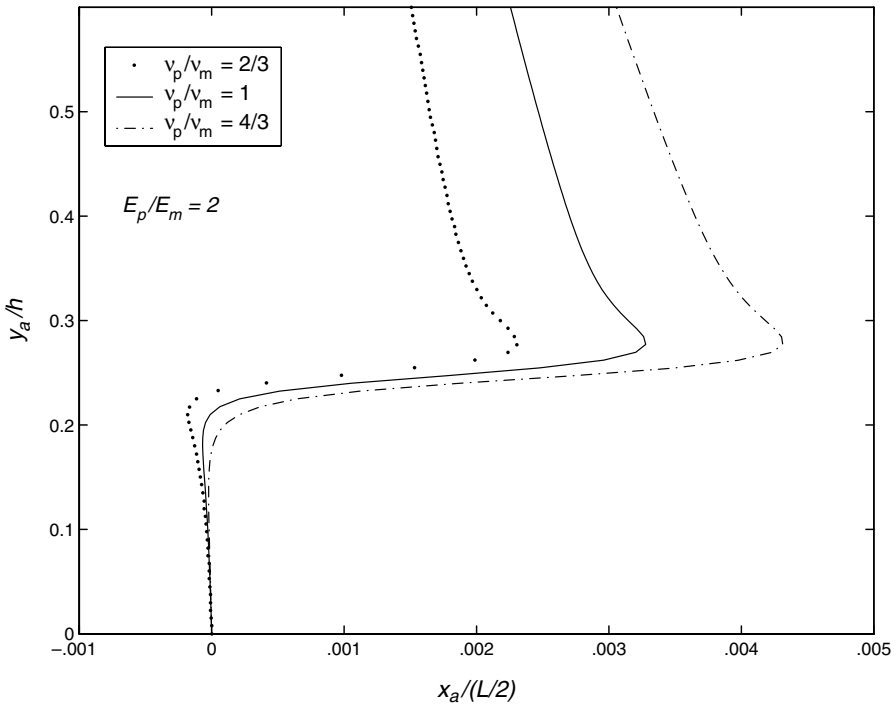


Fig. 7. Effects of $v_p/v_m$ on crack deflection due to single particle–crack interaction ($E_p/E_m = 2$).

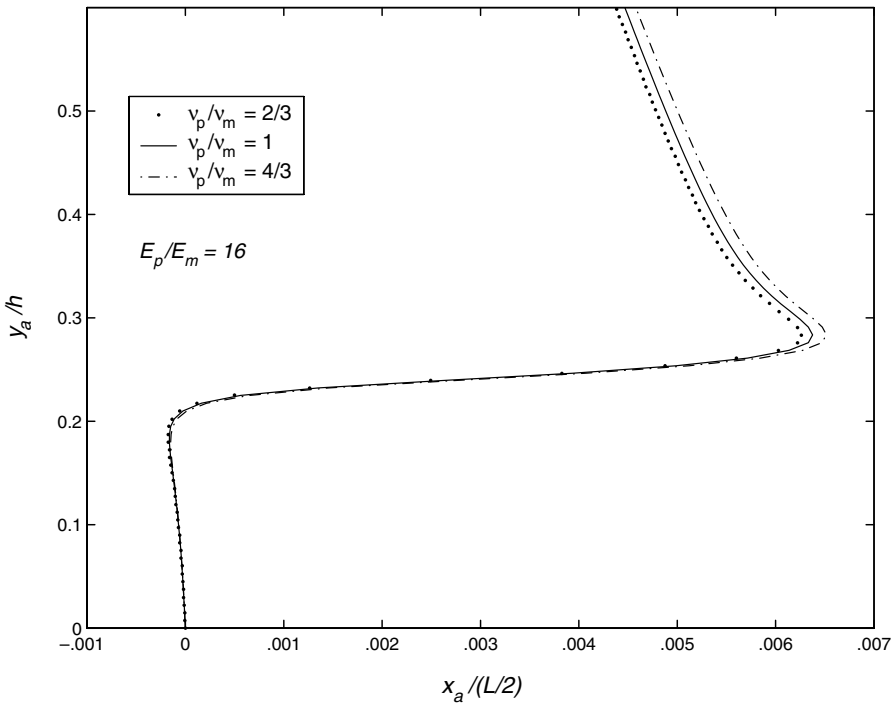


Fig. 8. Effects of $v_p/v_m$ on crack deflection due to single particle–crack interaction ($E_p/E_m = 16$).

varying $E_p/E_m$. The crack path does show a trend towards deflection away from nearby particles. However, the amount of deflection and its pattern is clearly not dictated solely by the near particles. The far particles'

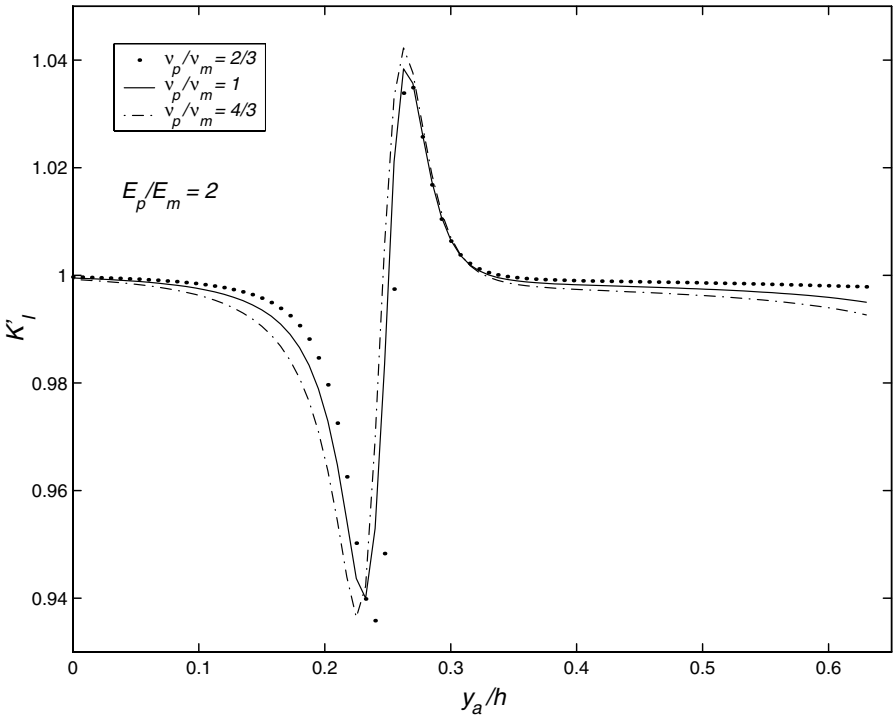


Fig. 9. Effects of $v_p/v_m$ on $K'_I$ due to single particle–crack interaction ($E_p/E_m = 2$).

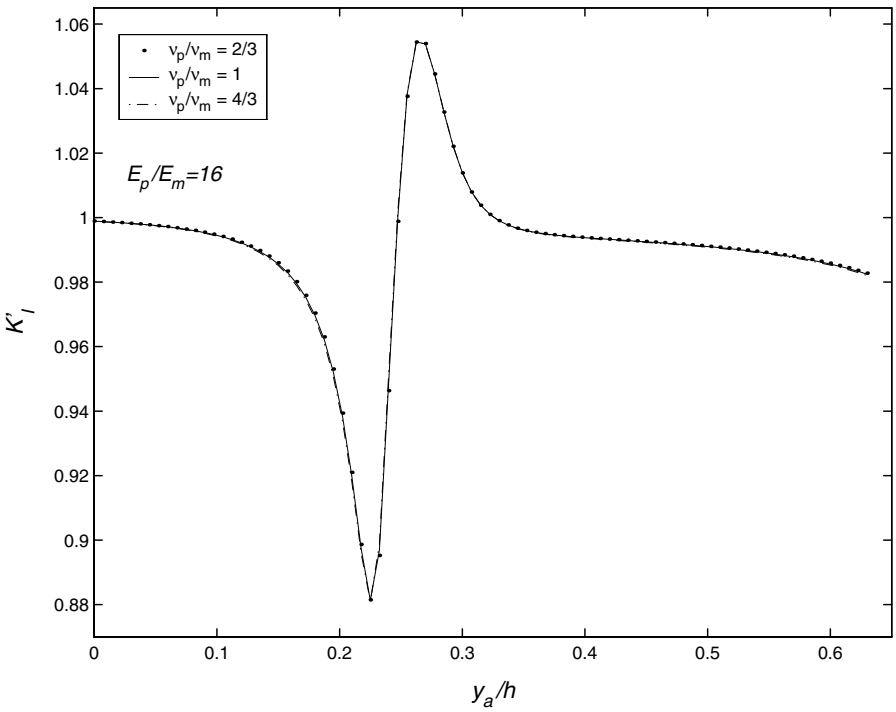


Fig. 10. Effects of $v_p/v_m$ on $K'_I$ due to single particle–crack interaction ($E_p/E_m = 16$).

influence becomes more and more evident as $E_p$ is increased, and one notices that the magnitude and pattern of crack deflection for $E_p/E_m = 16$ deviates from the trend seen with the lower values for $E_p/E_m$. The result is

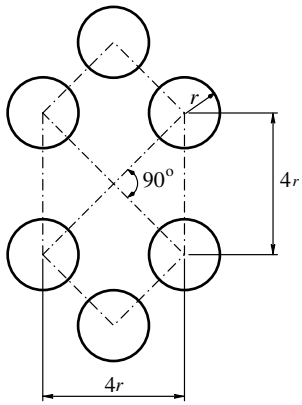


Fig. 11. Geometry of the aggregate.

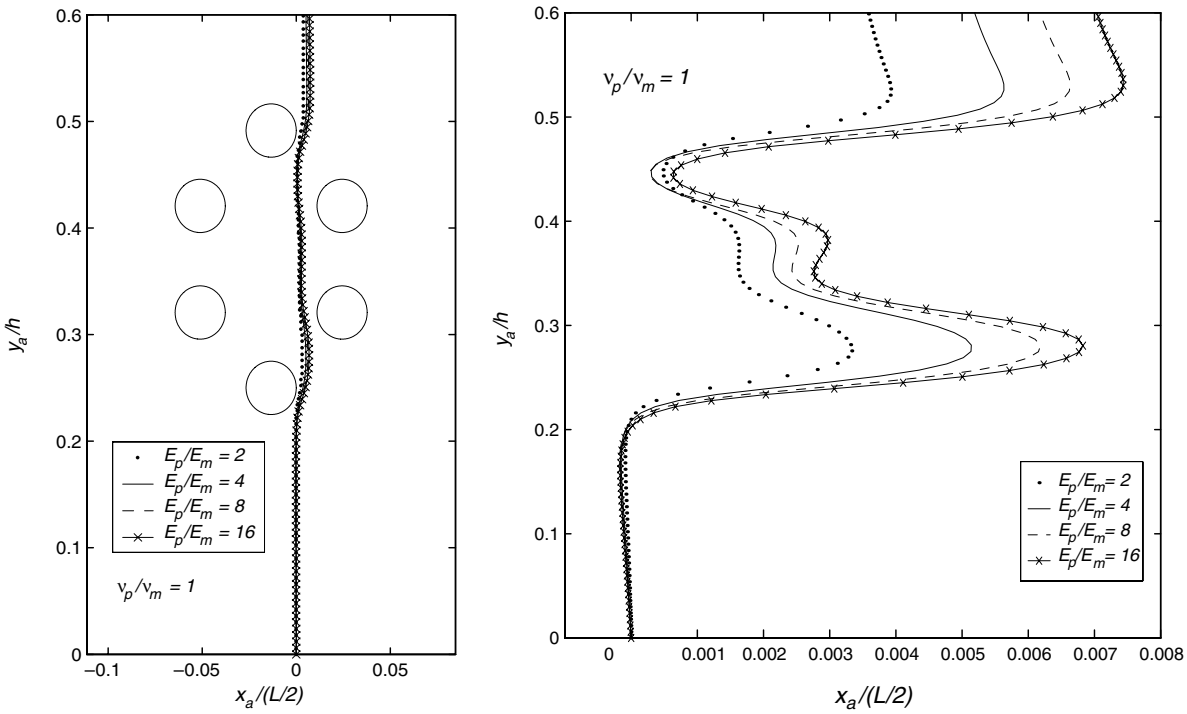


Fig. 12. Effects of $E_p/E_m$ on crack deflection due to aggregate–crack interaction. The right plot is a close-up view of the left one.

most likely due to the fact that increasing the Young's moduli of the particles has a similar effect to increasing the particles size, allowing for stronger competing and complementary interactions between the particles. The crack attraction, when the crack is far away from the particles, follows a similar pattern as the crack deflection. The crack attraction is seen to clearly increase with increasing $E_p/E_m$. However, when $E_p/E_m = 16$ a deviation from the tendency is observed.

For single inclusion simulations, it was shown that increasing $E_p$ had the effect of increasing the magnitudes of both $K_I$ amplification and reduction. With multiple inclusions present, one would assume competing and complementary interactions between the particles would affect the magnitude and trend of $K_I$. Fig. 13 substantiates this assumption. Increasing $E_p$ with the given inclusion pattern has the general effect of increasing $K_I$ amplification, resulting in a shift of the $K_I$ curve. However, it is clear that at various portions of the curves, one is evaluating the effects of more than one particle and that any observed trend is not absolute. For

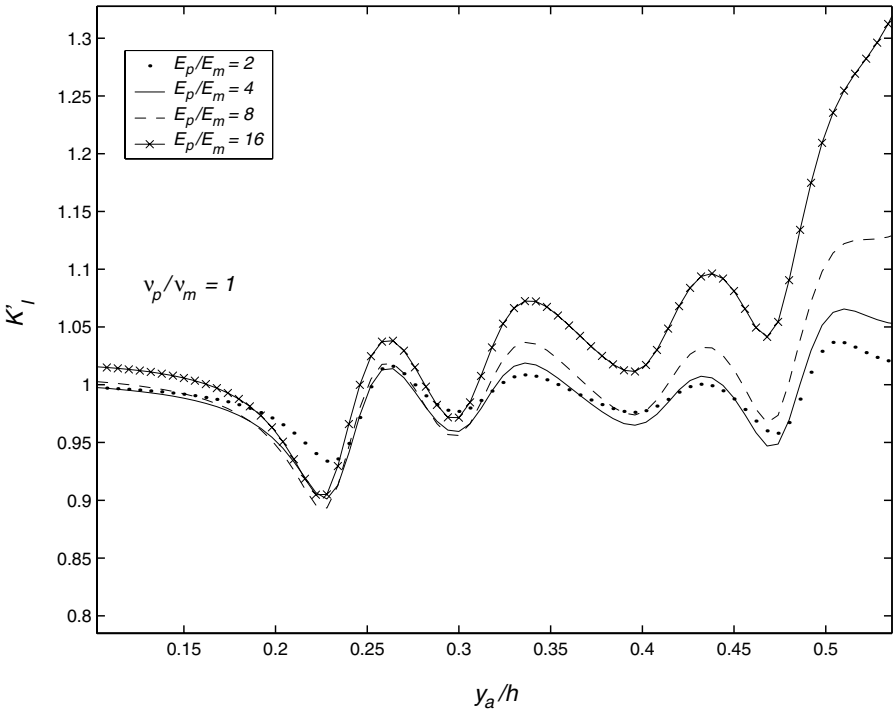


Fig. 13. Effects of $E_p/E_m$ on $K'_I$ due to aggregate–crack interaction.

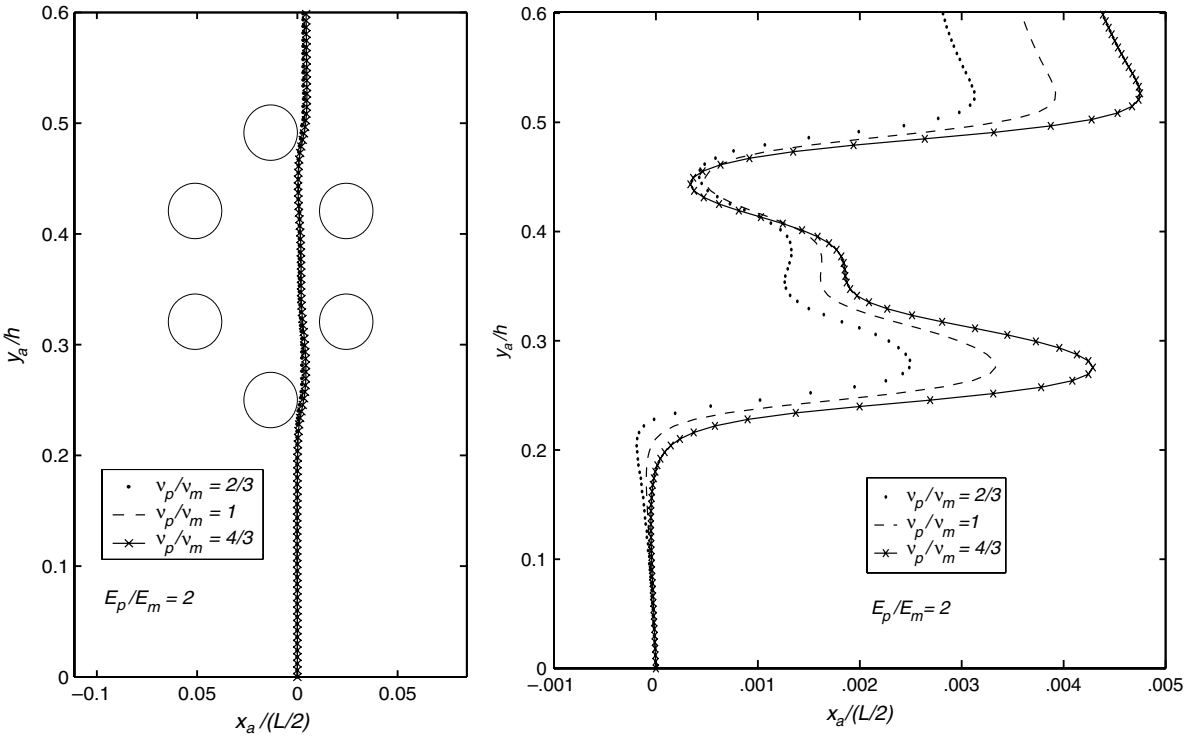


Fig. 14. Effects of $v_p/v_m$ on crack deflection due to aggregate–crack interaction ($E_p/E_m = 2$). The right plot is a close-up view of the left one.

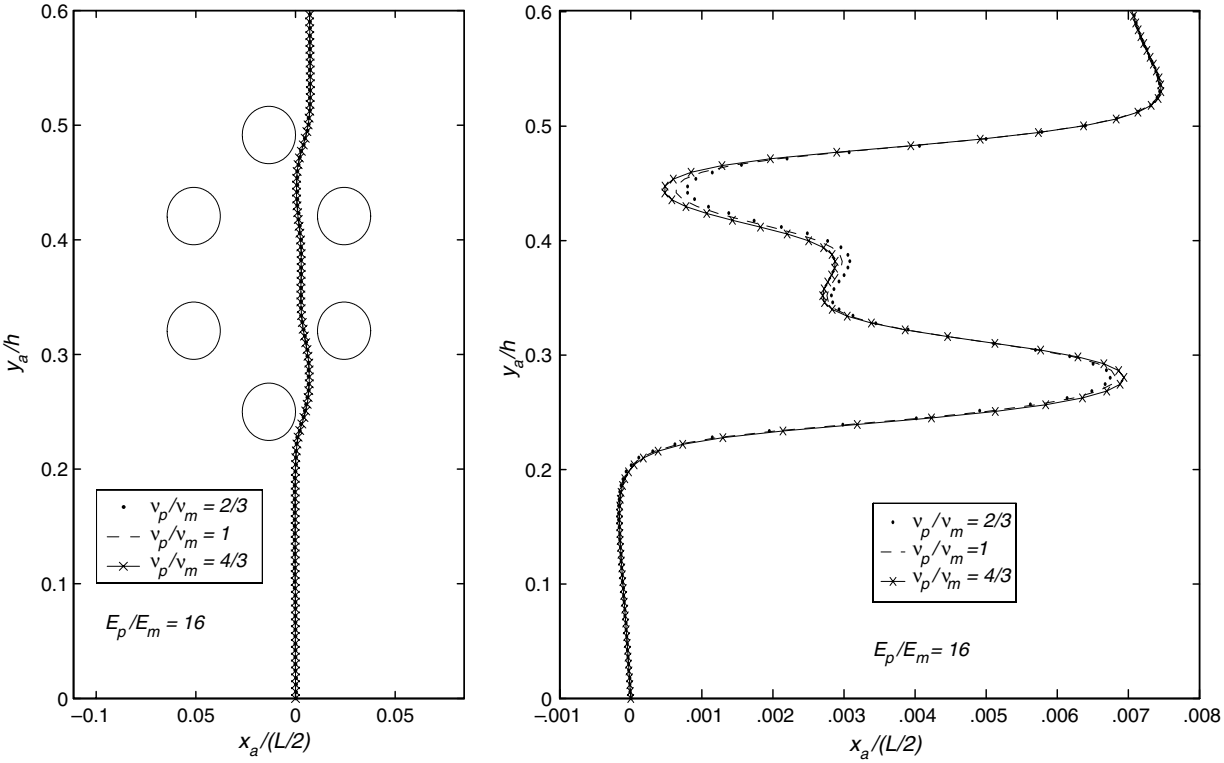


Fig. 15. Effects of $v_p/v_m$ on crack deflection due to aggregate–crack interaction ($E_p/E_m = 16$). The right plot is a close-up view of the left one.

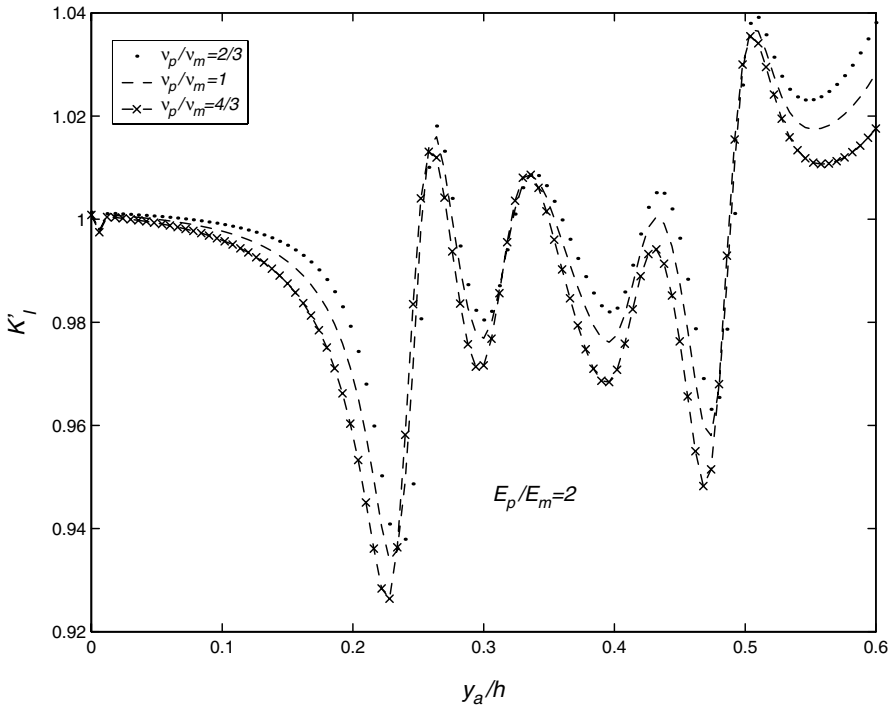


Fig. 16. Effects of $v_p/v_m$ on $K'_I$ due to aggregate–crack interaction ($E_p/E_m = 2$).

instance, there are sections of the $E_p/E_m = 16$ curve ($y_a/h = 0.3$) and sections of the $E_p/E_m = 2$ curve ($y_a/h = 0.4$) which deviate from the general trend. The deviation is most likely due to interactions between various particles and the crack. Considering the matrix and particle material properties in conjunction with aggregate geometry, particle number, and particle geometry it seems plausible to conclude that crack–particle interactions could potentially be manipulated in essentially infinite number of ways. Any formulation that seeks to fully describe the nature of the interactions between a crack and particle or aggregate of particles will be a complex function of the aforementioned variables.

### 3.5. Effects of $\nu_p/\nu_m$ on aggregate–crack interaction

The effects of a Poisson's ratio mismatch on a matrix material with multiple inclusions are considered in this section. Simulations are carried out for both relatively high and low $E_p/E_m$ ratios. The aggregate geometry is identical to that in Fig. 11. Fig. 14 shows the effects of the $\nu_p/\nu_m$ ratio on crack deflection with $E_p/E_m = 2$, while Fig. 15 show the effects of the $\nu_p/\nu_m$ ratio on crack deflection with $E_p/E_m = 16$. Fig. 16 shows the effects of the $\nu_p/\nu_m$ ratio on $K'_I$ with $E_p/E_m = 2$, while Fig. 17 shows the same effects with $E_p/E_m = 16$.

As with single inclusion simulations exploring the effects of the $\nu_p/\nu_m$, it is clear that the ratio has a greater effect at lower $E_p/E_m$ values. The general effect of increasing $\nu_p$ is an increase in crack deflection. However Fig. 14 indicates that the trend is not absolute as there are areas in which the plots with lower $\nu_p/\nu_m$ ratio appear to show more crack deflection than plots representing a higher $\nu_p/\nu_m$. The deviation does not occur in the case where $E_p/E_m = 16$. These results reinforce the fact that there is strong interplay between material constants, and emphasize the importance of considering the effects of material constants along with particle volume fraction and aggregate geometry. It also points out the necessity of understanding the situations in which certain properties become more relevant to the overall material behavior. The behavior for the crack attraction, before the crack reaches the particle, appears consistent for both values of $E_p/E_m$ considered and shows decreasing attraction to the particle with increasing $\nu_p/\nu_m$.

The $\nu_p/\nu_m$ ratio has the most influence on $K_I$ at lower values of $E_p/E_m$ (see Figs. 16 and 17). For $E_p/E_m = 16$ the most notable deviation between the $K_I$ curves is seen to be in the amplification peaks, whereas for

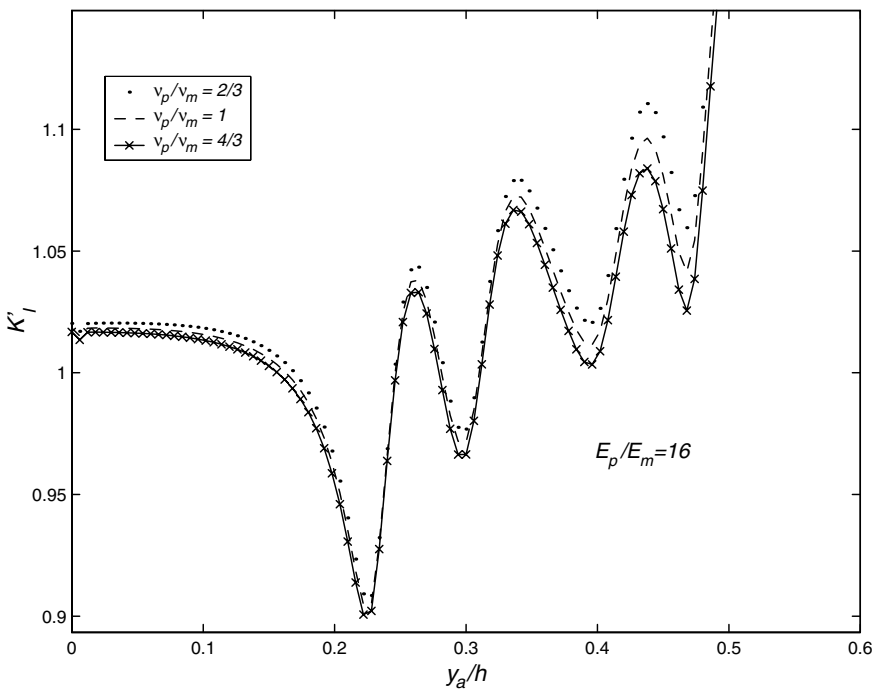


Fig. 17. Effects of $\nu_p/\nu_m$ on $K'_I$ due to aggregate–crack interaction ($E_p/E_m = 16$).

$E_p/E_m = 2$ the largest difference between the curves is in the reduction or shielding portions. The result implies that both the amount and nature of the influence that $\nu_p/\nu_m$ exerts varies with $E_p/E_m$. The higher value of $E_p/E_m$ yields more uniform behavior with varying $\nu_p$ than the lower value. In any case, it is clear that increasing $\nu_p/\nu_m$ allows the presence of the particles further away from the crack to be felt more strongly. It is interesting to note that, between ($y_a/h = 0.2$) and ($y_a/h = 0.5$), for $E_p/E_m = 16$, the overall $K_I$ value is steadily increasing whereas for $E_p/E_m = 2$, the overall $K_I$ value is steadily decreasing. Because the particle number, aggregate geometry, and variation of $\nu_p/\nu_m$ are constant between the two simulations, the results must be solely due to the differences in $E_p/E_m$. This observation reiterates how substantial the effects of various combinations of the material constants can be on crack growth behavior.

## 4. Concluding remarks

A SGBEM-based quasi-static crack growth prediction tool was developed and employed to investigate the effects material constants play in determining crack growth and $K_I$ behaviors in heterogeneous materials. It is demonstrated through validation that, by incorporating the MQP element into a multiregion SGBEM analysis, the code is able to produce accurate SIFs for problems involving crack–particle interactions. Simulations were carried out for both single and multiple inclusions. The Young's modulus and Poisson's ratio of the inclusion(s) were varied to affect the ratios $E_p/E_m$ and $\nu_p/\nu_m$, respectively. The principal results of the simulations are summarized as follows:

- An inclusion embedded in a relatively compliant matrix material causes crack deflection away from the inclusion when the crack is near the particle, and crack attraction towards the inclusion when the crack is relatively far from the particle. Increasing either $E_p/E_m$ or $\nu_p/\nu_m$ has the effect of increasing crack deflection away from the particle when the crack is close to it. However, when the crack is far from the inclusion, increasing $E_p/E_m$ causes an increase in the crack attraction towards the particle whereas increasing $\nu_p/\nu_m$ causes a decrease in the crack attraction.
- In general, the ratio $E_p/E_m$ appears to have the most overall influence on crack propagation and $K_I$. For low ratios of $E_p/E_m$, the effects of $\nu_p/\nu_m$ are extremely significant. At higher $E_p/E_m$ the effects of $\nu_p/\nu_m$ are detectable, but appear to be less significant. In regards to crack deflection, it could be said that increasing the ratio of the elastic constants has a general effect similar to shifting the particle closer to the initial crack-line/vertical axis of symmetry (a horizontal shift) or increasing the particle's/particles' size.
- The crack tip shielding and amplification were also observed, as in, i.e., [4,9]. Reduction and amplification of $K_I$ both increase in value with increases in the elastic constant ratios. Changes in the elastic constants appear to have a greater, positive influence on the reduction portion of the $K_I$ curve than the corresponding amplification portion (the amount of reduction is consistently greater than the amount of amplification).
- The presence of multiple inclusions causes complex complementary and competing interactions between the particles that strongly effect crack deflection and $K_I$. Overt trends can be seen in the deflection and $K_I$ behavior. However, the nature of the interactions between the crack and multiple inclusions makes any attempt to formulate an absolute characterization of the deflection and $K_I$ behaviors difficult.
- The results of multiple inclusion simulations indicate a complicated interaction strongly dictated by material constants. The simulation results naturally suggest the potential influence of particle number and spatial orientation. The aforementioned variables, taken collectively, could be manipulated in a seemingly infinite number of ways with the possibility to produce significantly varying results (at least in some cases). In order to formulate a definitive characterization of crack deflection and stress intensity behavior, inclusion number, material constants, and the relative orientation of the particles must all be considered.

## Acknowledgements

This research was supported in part by the Alabama Space Grant Consortium, NASA Training Grant NNG05GE80H to RCW, by the US Army Research Office Grant #W911 NF-04-1-0257 to HVT and A-VP, and by the Applied Mathematical Sciences Research Program of the Office of Mathematical,

Information, and Computational Sciences, the US Department of Energy under Contract DE-AC05-00OR22725 with UT-Battelle, LLC., to TK and LJG.

## References

[1] Tamate O. The effect of a circular inclusion on the stresses around a line crack in a sheet under tension. Int J Fract 1968;4:257–65.
[2] Sendeckyj GP. Interaction of cracks with rigid inclusions in longitudinal shear deformation. Int J Fract 1974;10:45–52.
[3] Hwu C, Liang YK, Yen WJ. Interactions between inclusions and various types of cracks. Int J Fract 1995;73:301–23.
[4] Li R, Chudnovsky A. Variation of the energy release rate as a crack approaches and passes through an elastic inclusion. Int J Fract 1993;59:R69–74.
[5] Li R, Chudnovsky A. Energy analysis of crack interaction with an elastic inclusion. Int J Fract 1993;63:247–61.
[6] Lipetzky P, Schmauder S. Crack–particle interaction in two-phase composites. Part I: Particle shape effects. Int J Fract 1994;65:345–58.
[7] Lipetzky P, Knesl Z. Crack–particle interaction in two-phase composites. Part II: Crack deflection. Int J Fract 1995;73:81–92.
[8] Haddi A, Weichert D. Three-dimensional interaction between a crack front and particles. Int J Numer Meth Engng 1998;42:1463–76.
[9] Bush MB. The interaction between a crack and a particle cluster. Int J Fract 1997;88:215–32.
[10] Knight MG, Wrobel LC, Henshall JL, De Lacerda LA. A study of the interaction between a propagating crack and an uncoated/coated elastic inclusion using the BE technique. Int J Fract 2002;114:47–61.
[11] Wang C, Libardi W, Baldo JB. Analysis of crack extension paths and toughening in a two phase brittle particulate composite by the boundary element method. Int J Fract 1998;94:177–88.
[12] Lei J, Wang Y-S, Gross D. Analysis of dynamic interaction between an inclusion and a nearby moving crack by BEM. Engng Anal Bound Elem 2005;29:802–13.
[13] Hartmann F. Introduction to boundary elements – theory and applications. Berlin: Springer Verlag; 1989.
[14] Blandford GE, Ingraffea AR, Liggett JA. Two-dimensional stress intensity factor computations using the boundary element method. Int J Num Meth Engng 1981;17:387–404.
[15] Bonnet M. Boundary integral equation methods for solids and fluids. England: John Wiley & Sons; 1995.
[16] Bonnet M, Maier G, Polizzotto C. On symmetric Galerkin boundary element method. ASME Appl Mech Rev 1998;51:669–704.
[17] Gray LJ. Evaluation of hypersingular integrals in the boundary element method. Math Comput Model 1991;15:165–74.
[18] Martin PA, Rizzo FJ. Hypersingular integrals: how smooth must the density be? Int J Num Meth Engng 1996;39:687–704.
[19] Henshell RD, Shaw KG. Crack tip finite elements are unnecessary. Int J Num Meth Engng 1975;9:495–507.
[20] Barsoum RS. On the use of isoparametric finite elements in linear fracture mechanics. Int J Num Meth Engng 1976;10:25–37.
[21] Banks-Sills L. Application of the finite element method to linear elastic fracture mechanics. Appl Mech Rev 1991;44:447–61.
[22] Gray LJ, Paulino GH. Crack tip interpolation, revisited. SIAM J Appl Math 1998;58:428–55.
[23] Gray LJ, Phan A-V, Paulino GH, Kaplan T. Improved quarter-point crack tip element. Engng Fract Mech 2003;70:269–83.
[24] Erdogan F, Sih GC. On the crack extension in plates under plane loading and transverse shear. J Basic Engng 1963;86:519–27.
[25] Rizzo FJ. An integral equation approach to boundary value problems of classical elastostatics. Quart Appl Mathemat 1967;25:83–95.
[26] Maier G, Diligenti M, Carini A. A variational approach to boundary element elastodynamic analysis and extension to multidomain problems. Comp Meth Appl Engng 1991;92:93–213.
[27] Hölzer SM. How to deal with hypersingular integrals in the symmetric BEM. Comm Num Meth Engng 1993;9:219–32.
[28] Gray LJ, Paulino GH. Symmetric Galerkin boundary integral formulation for interface and multi-zone problems. Int J Num Meth Engng 1997;40:3085–101.
[29] Williams ML. Stress singularities resulting from various boundary conditions in angular corners of plates in extension. ASME J Appl Mech 1952;19:526–8.
[30] Williams ML. On the stress distribution at the base of a stationary crack. ASME J Appl Mech 1957;24:109–14.
[31] Martin PA. End-point behavior of solutions to hypersingular equations. Proc R Soc London A 1991;432:301–20.
[32] Sih GC. Strain energy density factor applied to mixed mode crack problems. Int J Fract 1974;10:305–21.
[33] Erdogan F, Gupta GD, Ratwani M. Interaction between a circular inclusion and an arbitrarily oriented crack. J Appl Mech 1974;41:1007–13.